

Enhanced upper ocean warming projected by the eddy-resolving Community Earth System Model

Gaopeng Xu¹, Chang Ping¹, Justin Small², Gokhan Danabasoglu³, Stephen Yeager⁴, Qiuying Zhang¹, and Sanjiv Ramachandran⁵

¹Texas A&M University

²National Center for Atmospheric Research (UCAR)

³National Center for Atmospheric Research (NCAR)

⁴National Center for Atmospheric Research

⁵Texas A & M University

August 31, 2023

Abstract

Ocean warming is a key factor impacting future changes in climate. Here we investigate vertical structure changes in globally averaged ocean heat content (OHC) in high- (HR) and low-resolution (LR) future climate simulations with the Community Earth System Model (CESM). Compared with observation-based estimates, the simulated OHC anomalies in the upper 700 m and 2000 m during 1960-2020 are more realistic in CESM-HR than -LR. Under RCP8.5 scenario, the net surface heat into the ocean is very similar in CESM-HR and -LR. However, CESM-HR has a larger increase in OHC in the upper 250 m compared to CESM-LR, but a smaller increase below 250 m. This difference can be traced to differences in eddy-induced vertical heat transport between CESM-HR and -LR in the historical period. Moreover, our results suggest that with the same heat input, upper-ocean warming is likely to be underestimated by most non-eddy-resolving climate models.

Hosted file

972375_0_art_file_11330464_s04dck.docx available at <https://authorea.com/users/530053/articles/662469-enhanced-upper-ocean-warming-projected-by-the-eddy-resolving-community-earth-system-model>

1 **Enhanced upper ocean warming projected by the eddy-resolving Community Earth System**
2 **Model**

3 **Gaopeng Xu¹, Ping Chang^{1,2}, Justin Small³, Gokhan Danabasoglu³, Stephen Yeager³,**
4 **Sanjiv Ramachandran¹, and Qiying Zhang¹**

5 ¹Department of Oceanography, Texas A&M University, College Station, Texas, USA

6 ²Department of Atmospheric Sciences, Texas A&M University, College Station, Texas, USA

7 ³National Center for Atmospheric Research, Boulder, Colorado, USA.

8

9

10 Corresponding author: Gaopeng Xu (gaopxu@tamu.edu)

11

12

13

14 **Key points**

- 15 • Simulated upper-ocean ocean heat content anomalies are more realistic in high-resolution
16 simulations than in low-resolution counterparts.
- 17 • With similar ocean surface heating, high-resolution simulations project stronger upper-
18 ocean warming than low-resolution simulations.
- 19 • Future changes in vertical heat transport depend on the representation of the mean ocean
20 states at present day.

21

22

23

24

25

26

27

28

29

30

31

32

33

34 Abstract

35 Ocean warming is a key factor impacting future changes in climate. Here we investigate vertical
36 structure changes in globally averaged ocean heat content (OHC) in high- (HR) and low-
37 resolution (LR) future climate simulations with the Community Earth System Model (CESM).
38 Compared with observation-based estimates, the simulated OHC anomalies in the upper 700 m
39 and 2000 m during 1960-2020 are more realistic in CESM-HR than -LR. Under RCP8.5 scenario,
40 the net surface heat into the ocean is very similar in CESM-HR and -LR. However, CESM-HR
41 has a larger increase in OHC in the upper 250 m compared to CESM-LR, but a smaller increase
42 below 250 m. This difference can be traced to differences in eddy-induced vertical heat transport
43 between CESM-HR and -LR in the historical period. Moreover, our results suggest that with the
44 same heat input, upper-ocean warming is likely to be underestimated by most non-eddy-
45 resolving climate models.

46 Plain language summary

47 With the rise in anthropogenic emissions, the ocean has absorbed over 90% of greenhouse gas-
48 related heat, resulting in well-known ocean warming. This warming is the main cause of severe
49 deoxygenation, coral bleaching, and sea-level rise, among others. Furthermore, the upper ocean
50 experiences more warming than the deep ocean, which leads to strengthened ocean stratification.
51 On a global scale, the heat into the ocean is vertically redistributed by a downward mean-flow-
52 induced heat transport, upward eddy-induced heat transport, and vertical turbulent mixing. In this
53 study, we compare vertical structures of ocean heat uptake in response to anthropogenic forcing
54 between high (~10 km) and low horizontal resolution (~100 km) future climate simulations. We
55 find that, with similar heat input at the ocean surface, the high-resolution simulations exhibit
56 more warming in the upper 250 m of the ocean than their low-resolution counterparts. This
57 difference is caused by the different representations of vertical heat transport by mesoscale ocean
58 eddies in high- and low-resolution models.

59 1. Introduction

60 The increase in anthropogenic greenhouse gas (GHG) emissions has led to an increase in ocean
61 stratification due to uneven warming at different depths (Capotondi et al., 2012; Li et al., 2020;
62 Yamaguchi & Suga, 2019). This trend is projected to continue (Bopp et al., 2013; Moore et al.,
63 2018), and could negatively impact the deep ocean's ability to absorb carbon dioxide from the
64 atmosphere (Bourgeois et al., 2022). Moreover, warmer seawater holds less soluble oxygen, and
65 the enhanced ocean stratification weakens oxygen exchanges between the upper and deep ocean
66 (Helm et al., 2011; Keeling et al., 2010; Schmidtke et al., 2017), resulting in reduced net primary
67 and export production (Fu et al., 2016). In addition, ocean warming is responsible for coral
68 bleaching (Bleuel et al., 2021; Cantin et al., 2010; Frieler et al., 2013), poleward shifts of fish
69 species (Perry et al., 2005; Pinsky et al., 2013), and sea level rise (Church et al., 2011;
70 Domingues et al., 2008; Levitus et al., 2012). It is, therefore, imperative to improve our
71 capability to skillfully project future changes in upper-ocean warming.

72 Observational studies have shown that more than 90% of heat generated by human activities has
73 been absorbed by the ocean during the historical period (Cheng et al., 2019; Gattuso et al., 2015;
74 Rhein et al., 2013; Trenberth et al., 2014), with around 87% of it stored in the upper 2000 m
75 (Cheng et al., 2017). This heat has mainly been distributed in the upper 700 m prior to 1990 and
76 has gradually moved into the deep ocean in the more recent period (Chen & Tung, 2014; Cheng
77 et al., 2017). However, projecting future changes in ocean temperature directly from these
78 observations remains challenging due to the short record length and large natural climate
79 variability. Climate models have, therefore, become crucial tools for understanding and
80 predicting future ocean warming and stratification.

81 Modeling studies have demonstrated that vertical heat transport (VHT) along with vertical
82 turbulent-mixing-induced heat fluxes plays a critical role in determining the vertical distribution
83 of ocean heat and consequently influencing ocean stratification (Griffies et al., 2015; Wolfe et al.,
84 2008). VHT encompasses upward eddy-induced heat transport (EVHT) and downward mean-
85 flow-induced heat transport (MVHT). EVHT tends to increase upper ocean temperature, while
86 MVHT tends to decrease it. Therefore, accurately representing these ocean processes in climate
87 models is essential for simulating and projecting future changes in ocean stratification.

88 However, most of climate models used in the Coupled Model Intercomparison Project Phase 5
89 (CMIP5) do not explicitly resolve ocean eddies due to their low horizontal resolution of
90 approximately 1° . Instead, they parameterize eddy-induced heat fluxes (Fox-Kemper et al., 2008;
91 Gent & McWilliams, 1990). Previous studies (Flato et al., 2013; Kuhlbrodt & Gregory, 2012)
92 have shown that these models generally exhibit less stratification compared to observations in
93 the upper 2000 m. In contrast, recent investigations (Chang et al., 2020) based on simulations
94 using the Community Earth System Model (CESM) have revealed that explicitly representing
95 mesoscale eddies by increasing the ocean model's horizontal resolution to approximately 0.1°
96 enhances global-mean ocean stratification, especially in the upper 1000 m. Similar findings have
97 been seen in other high-resolution climate model studies (Griffies et al., 2015; Roberts et al.,
98 2019). The mean ocean stratification has been further shown to constrain heat uptake efficiency
99 in the Southern Ocean (Bourgeois et al., 2022). These results motivate us to investigate whether
100 the representation of explicitly resolved versus parameterized eddy fluxes in high- and low-
101 resolution climate models, respectively, is the primary factor contributing to such differences in
102 future projections of global ocean stratification changes through modulating vertical heat
103 distributions.

104 **2. Data and Methods**

105 **2.1 CESM simulations**

106 Both the high- and low-resolution CESM (CESM-HR and CESM-LR, respectively) simulations
107 used in this study were performed using CESM version 1.3 (Chang et al., 2020, 2023; Meehl et
108 al., 2019; Small et al., 2014). In the present study, we make use of the following CESM-HR
109 simulations: a 500-year-long pre-industrial control (PI-CNTL) simulation run under constant
110 1850 forcing conditions; a historical-future transient (HF-TNST) simulation for the 1850-2100
111 period that started from year 250 of PI-CNTL; and two additional HF-TNST ensemble members
112 for the 1920-2100 period, which were branched from the 1850-2100 HF-TNST at year 1920 with

113 roundoff-level perturbations added to the atmospheric potential temperature initial conditions.
 114 These HF-TNST simulations use historical forcings from 1850 to 2005, followed by RCP8.5
 115 forcings from 2006 to 2100. We also employ the corresponding LR simulations which have 5
 116 HF-TNST ensemble members.

117 OHC change (ΔOHC) is defined as the OHC in HF-TNST after subtracting the linear trend of
 118 OHC in PI-CNTL, to ensure that the impact of model drift is largely removed (see Section 2.3
 119 below). This approach assumes that the model drift remains unchanged in both HF-TNST and
 120 PI-CNTL. In addition, this study defines eddies as the departure from seasonal-mean in CESM-
 121 HR to construct eddy vertical heat transport (EVHT). However, conclusions will keep the same
 122 if using monthly mean to define eddy. The EVHT change (ΔEVHT) is defined as the difference
 123 between mean EVHT in HF-TNST and PI-CNTL.

124 2.2 Observation-based data and CMIP5 simulations

125 To validate the CESM simulations during the historical period from 1960 to 2020, we compare
 126 them with observation-based ocean heat content (OHC) estimates from three different sources:
 127 Institute of Atmospheric Physics (IAP) (Cheng et al., 2017), Japan Meteorological Agency
 128 (JMA) (Ishii et al., 2017), and NOAA (Levitus et al., 2012). In addition, 20 coupled climate
 129 models participating in CMIP5 (see Table S1) are used to compare with CESM results. In the
 130 comparative analysis, we made a deliberate decision not to include CMIP6 simulations due to
 131 potential complications arising from different emission forcings used in CESM-HR and CMIP6
 132 simulations.

133 2.3 Heat Budget Analysis

134 The potential temperature equation in Cartesian coordinates is given by

$$135 \frac{\partial T}{\partial t} = -\frac{\partial(uT)}{\partial x} - \frac{\partial(vT)}{\partial y} - \frac{\partial(wT)}{\partial z} + \frac{1}{c_P \rho_0} \frac{\partial Q}{\partial z} + \kappa_H \left(\frac{\partial^2}{\partial x^2} + \frac{\partial^2}{\partial y^2} \right) T + \frac{\partial}{\partial z} \kappa_v \left(\frac{\partial T}{\partial z} - \gamma_x \right), \quad (1)$$

136 where T is the potential temperature; u , v , and w are the total velocity components along the x
 137 (longitude), y (latitude), and z (vertical; positive upwards) axes; Q is the heat flux (positive
 138 downward) including solar and nonsolar components; $c_P=3996$ J/kg/°C is the heat capacity of
 139 seawater; ρ_0 is the density of seawater taken as 1026 kg/m³; κ_H and κ_v are the horizontal and
 140 vertical diffusivities; γ_x represents the nonlocal term in the K-Profile Parameterization (KPP)
 141 (Large et al., 1994). On the right-hand side (RHS) of Eq. 1, the first three terms represent the
 142 convergence of total heat transport, which includes resolved and parameterized heat transport in
 143 CESM-LR and only the resolved heat transport in CESM-HR. The remaining terms denote the
 144 atmospheric heating and horizontal and vertical turbulent mixing, respectively.

145 After integrating Eq. 1 in latitude and longitude space over the global ocean, all horizontal
 146 oceanic processes vanish, and the equation reduces to:

$$147 \frac{\partial \langle T \rangle}{\partial t} = -\frac{\partial \langle wT \rangle}{\partial z} + \frac{1}{c_P \rho_0} \frac{\partial \langle Q \rangle}{\partial z} + \frac{\partial}{\partial z} \left\langle \kappa_v \left(\frac{\partial T}{\partial z} - \gamma_x \right) \right\rangle, \quad (2)$$

148 where the angle bracket $\langle \cdot \rangle$ represents the horizontal integration operator. The evolution of the
 149 global-mean temperature can be obtained by integrating Eq. 2 in time:

$$150 \quad \langle T(z, t) \rangle - \langle T(z, 0) \rangle = \int_0^t \frac{-\partial \langle wT \rangle}{\partial z} dt + \int_0^t \frac{1}{c_P \rho_0} \frac{\partial \langle Q \rangle}{\partial z} dt + \int_0^t \frac{\partial}{\partial z} \left\langle \kappa_v \left(\frac{\partial T}{\partial z} - \gamma_x \right) \right\rangle dt. \quad (3)$$

151 After multiplying Eq. 3 by $c_P \rho_0$ and integrating between a given depth h below the ocean surface
 152 (below the shortwave penetration depth) and the seafloor H , the equation governing OHC from
 153 H to h is

$$154 \quad \langle OHC(t) \rangle - \langle OHC(0) \rangle = -c_P \rho_0 \int_0^t \langle wT \rangle|_{z=-h} dt + c_P \rho_0 \int_0^t \left\langle \kappa_v \left(\frac{\partial T}{\partial z} - \gamma_x \right) \right\rangle|_{z=-h} dt,$$

155 (4)

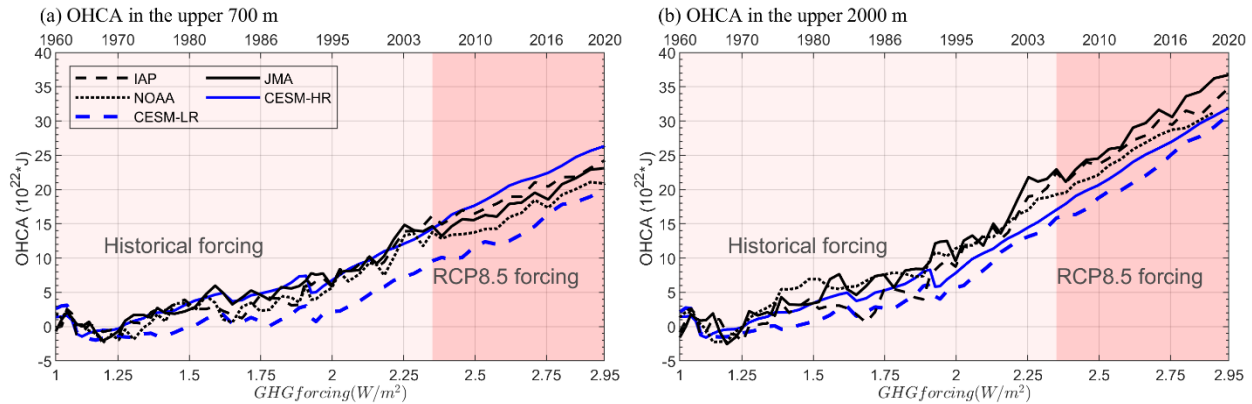
156 where the term on the left-hand side (LHS) of Eq. 4 is a timeseries of OHC ($c_P \rho_0 \int_{-H}^{-h} \langle T(z, t) \rangle dz$)
 157 anomaly relative to its value at $t=0$. The terms on the RHS are contributions from the global-
 158 mean VHT and vertical mixing at $z=-h$. The surface heat flux term in Eq. 3 does not appear in Eq.
 159 4 because the net atmospheric heating, including the penetrative shortwave radiation, is zero at
 160 depths of interest in this study, e.g., below 250 m. In the following analysis, the vertical turbulent
 161 mixing term will be calculated as a residual of the other terms in Eq. 4.

162 To compute the OHC response to greenhouse gas forcing, we first calculate each term in Eq. 4 in
 163 both PI-CNTL and HF-TNST, and then perform a linear regression analysis to each term in PI-
 164 CNTL. Finally, we subtract the PI-CNTL linear trend from each term of Eq. 4 in HF-TNST to
 165 remove the impact of model drift.

166 3. Results

167 3.1 Simulated OHC against observation-based estimates

168 Following Levitus et al. (2012), we first validate simulated OHC against observation-based
 169 estimates for the upper 700 m and upper 2000 m. In the upper 700 m, the OHC anomaly
 170 (OHCA), defined as departure from the mean over the period of 1960-1970, shows a broad
 171 agreement among the three observation-based products with values reaching $21 \times 10^{22} \sim 25 \times 10^{22}$ J
 172 at the end of 2020 (Fig. 1). CESM-HR agrees better with these products than CESM-LR during
 173 1960-2005, but CESM-HR (CESM-LR) overestimates (underestimates) OHCA during 2006-
 174 2020. The warming rate of OHC in the upper 700 m from 1960-2020 is 0.37 W/m^2 in CESM-HR
 175 and 0.26 W/m^2 in CESM-LR. The observation-based estimates of $0.31\text{-}0.35 \text{ W/m}^2$, consistent
 176 with those reported in the IPCC reports (Bindoff et al., 2019), are closer to the value in CESM-
 177 HR than that in CESM-LR.



178

179 **Fig. 1. OHCA in observation-based estimates and CESM.** (a) OHCA in the upper 700 m and
 180 (b) 2000 m estimated by IAP (black dashed), JMA (black solid), NOAA (black dotted), CESM-
 181 HR (blue solid), and CESM-LR (dashed blue). Baseline is the mean over 1960-1970. The bottom
 182 x-axis shows the GHG-induced radiative forcing (Wm^{-2}) under RCP8.5 emission scenario and
 183 the top x-axis shows the corresponding time (years).

184 In contrast to OHCA in the upper 700 m, the simulated OHCA in the upper 2000 m tends to be
 185 lower than those of the observation-based products in both CESM-HR and CESM-LR,
 186 particularly after the 1991 Mount Pinatubo eruption. However, CESM-HR values are
 187 consistently higher than those of CESM-LR and closer to the observation-based estimates.
 188 Interestingly, the difference in OHCA between CESM-HR and CESM-LR in the upper 2000 m is
 189 smaller than that in the upper 700 m, especially after early 1990s, suggesting some cancellation
 190 of differences above and below 700 m. The estimated warming rate of OHC in the upper 2000 m
 191 from 1960-2020 is between 0.46 and 0.53 W/m^2 in observation-based data, 0.45 W/m^2 in CESM-
 192 HR, and 0.42 W/m^2 in CESM-LR.

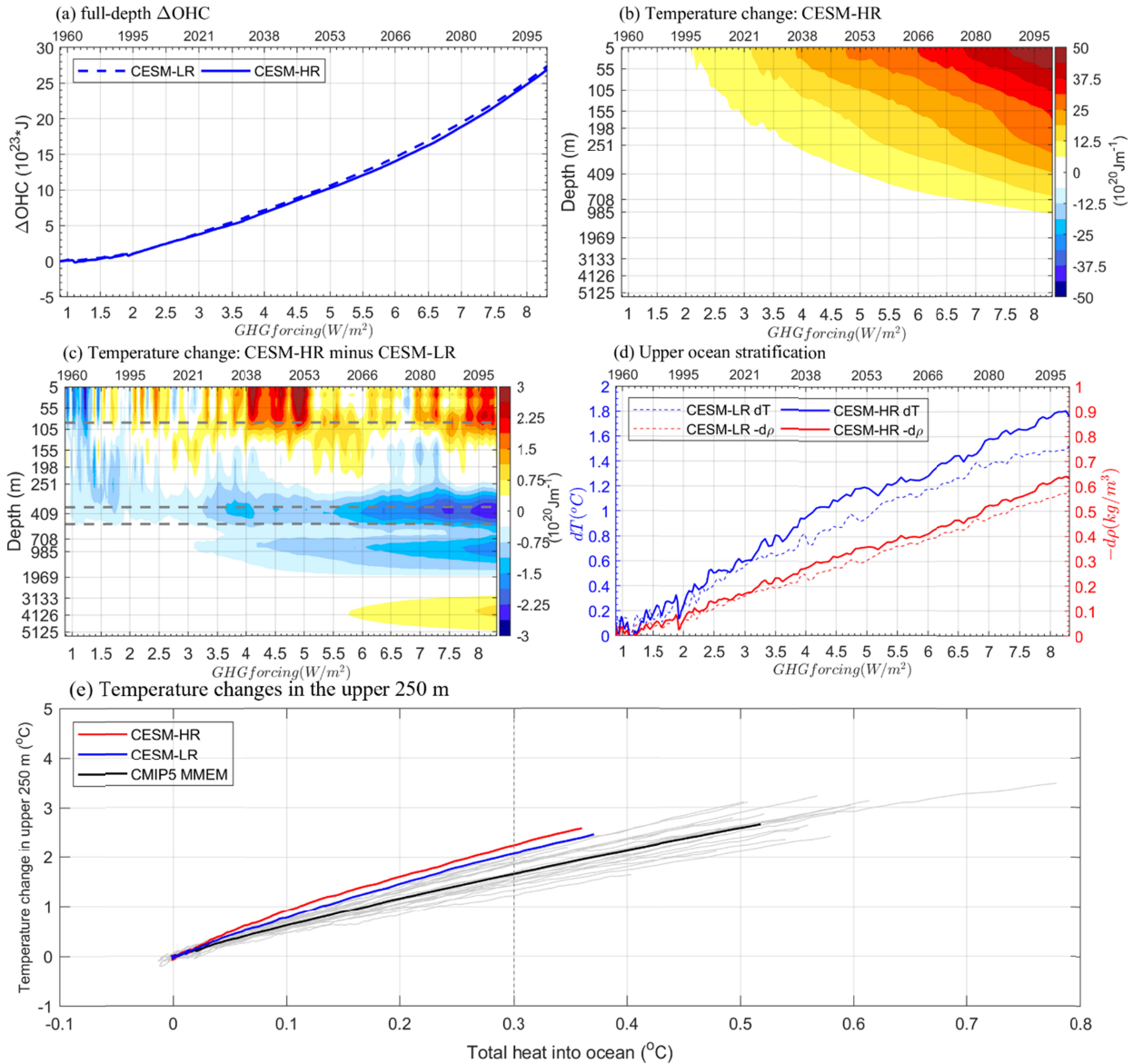
193 After comparing the simulated OHC in CESM-HR and CESM-LR against observation-based
 194 estimates, we can conclude that both models perform reasonably well in reproducing OHCA
 195 over the historical period in the upper ocean, with CESM-HR being closer to the observation-
 196 based estimates than CESM-LR. Moving forward, our focus will be on analyzing the projected
 197 future changes in OHC in both model configurations and assessing the impact of model
 198 resolution on global ocean warming and associated stratification changes.

199 3.2 Globally-averaged ocean temperature projections

200 The full-depth integrated global-mean ΔOHC in CESM-HR and CESM-LR closely aligns with
 201 each other from 1950 to 2100 (Fig. 2a), suggesting that horizontal resolution differences in
 202 CESM have a negligible impact on the total ocean heat uptake. Under RCP8.5 forcing, both
 203 CESM-HR and CESM-LR project a warming rate of 2.56 W/m^2 over the 2020-2100 period, with
 204 a net ocean heat uptake of 27×10^{23} J by the end of 2100, representing a sevenfold increase from
 205 2020. Because the total ocean heat uptake is directly related to the accumulated net surface heat
 206 flux over the global ocean, it means that CESM-HR and CESM-LR simulate remarkably similar
 207 amounts of net heat input into the ocean, despite their resolution differences. However, this does

208 not indicate that the vertical distribution of the ocean heat uptake will also be similar between
 209 CESM-HR and CESM-LR.

210



211

212 **Fig. 2. Projected ocean temperature changes in CESM and CMIP5 models.** (a) Full-depth
 213 integrated ΔOHC in CESM-LR (dashed) and CESM-HR (solid); (b) ocean temperature changes
 214 (scaled with horizontal ocean areas, c_p and ρ_0) as a function of depth in CESM-HR; (c) similar to
 215 (b) but for CESM-HR minus CESM-LR; (d) upper ocean temperature difference between 0-100
 216 m and 350-450 m (dT , blue; left axis) and upper ocean density difference ($-d\rho$, red; right axis) in
 217 CESM-LR (dashed) and CESM-HR (solid), with positive values indicating increases in
 218 stratification. Note that the y-axis in (b-c) is a linear function of vertical layer number in CESM,
 219 instead of depth. Grey dashed lines in (c) represent depths of 100 m, 350 m, and 450 m,
 220 respectively. The bottom x-axis shows the GHG-induced radiative forcing (Wm^{-2}) under RCP8.5

221 emission scenario and the top x-axis shows the corresponding time (years) starting from the year
222 1950. Results in (b-c) with the unit of °C are shown in Fig. S1a-b, respectively. (e) Relationship
223 of total heat into ocean and temperature changes (relative to the mean over 1950-1960) in the
224 upper 250 m. Red, blue, gray, and black lines in (e) represent results from CESM-HR, CESM-
225 LR, CMIP5 models, and CMIP5 multi-model ensemble mean (MMEM), respectively. CMIP5
226 models are forced by RCP8.5 from 2006-2100.

227

228 Fig. 2b shows global-mean ocean temperature changes relative to its PI-CNTL as a function of
229 depth and time in CESM-HR. The warming is relatively weak before 2000 with less than 2.1
230 W/m^2 of GHG-induced radiative forcing. The warm temperature anomaly gradually penetrates
231 deeper, reaching a depth of about 1000 m by the end of 2100, indicating an increase in the upper
232 ocean thermal stratification in the future as expected. These warming characteristics in CESM-
233 HR also hold in CESM-LR (Fig. S1), except that less warming is observed in the upper 250 m,
234 but more below 250 m in CESM-LR than in CESM-HR (Fig. 2c). We note that there are strong
235 internal variabilities in the upper 250 m. After using the signal-to-noise-maximizing EOF filter to
236 reduce internal variability (Wills et al., 2020), the stronger warming of the upper 250 m in
237 CESM-HR is more evident compared to CESM-LR (Fig. S2c). This result indicates that the
238 GHG-induced heat is moved into the deep ocean at a faster rate in CESM-LR than in CESM-HR.
239 Therefore, future changes in ocean stratification projected by CESM-HR and CESM-LR are
240 different.

241 Upper ocean thermal (density) stratification changes can be estimated by taking the difference
242 between potential temperature (density) averaged over the top 100 m and that over 350-450 m,
243 denoted as dT ($-d\rho$). These depth ranges are chosen mainly because the temperature differences
244 between CESM-HR and CESM-LR peak within these depth ranges (Fig. S3). As expected, dT is
245 increasing faster in CESM-HR than CESM-LR (Fig. 2d). Over the period of 2090-2100, the dT
246 increase in CESM-HR is more than 20% higher than that in CESM-LR. The overall increasing
247 trend of dT from 1950 to 2100 is 19% larger in CESM-HR than CESM-LR. This confirms that
248 increasing horizontal resolution in CESM does have an impact on the representations of upper-
249 ocean thermal stratification changes in the future. Upper-ocean density stratification changes,
250 estimated by $-d\rho$, follow closely the dT changes (Fig. 2d), indicating that density stratification
251 changes are dominated by temperature changes globally, in agreement with observation-based
252 results (Li et al., 2020). These results are also more evident after applying signal-to-noise-
253 maximizing EOF filter (Fig. S2d).

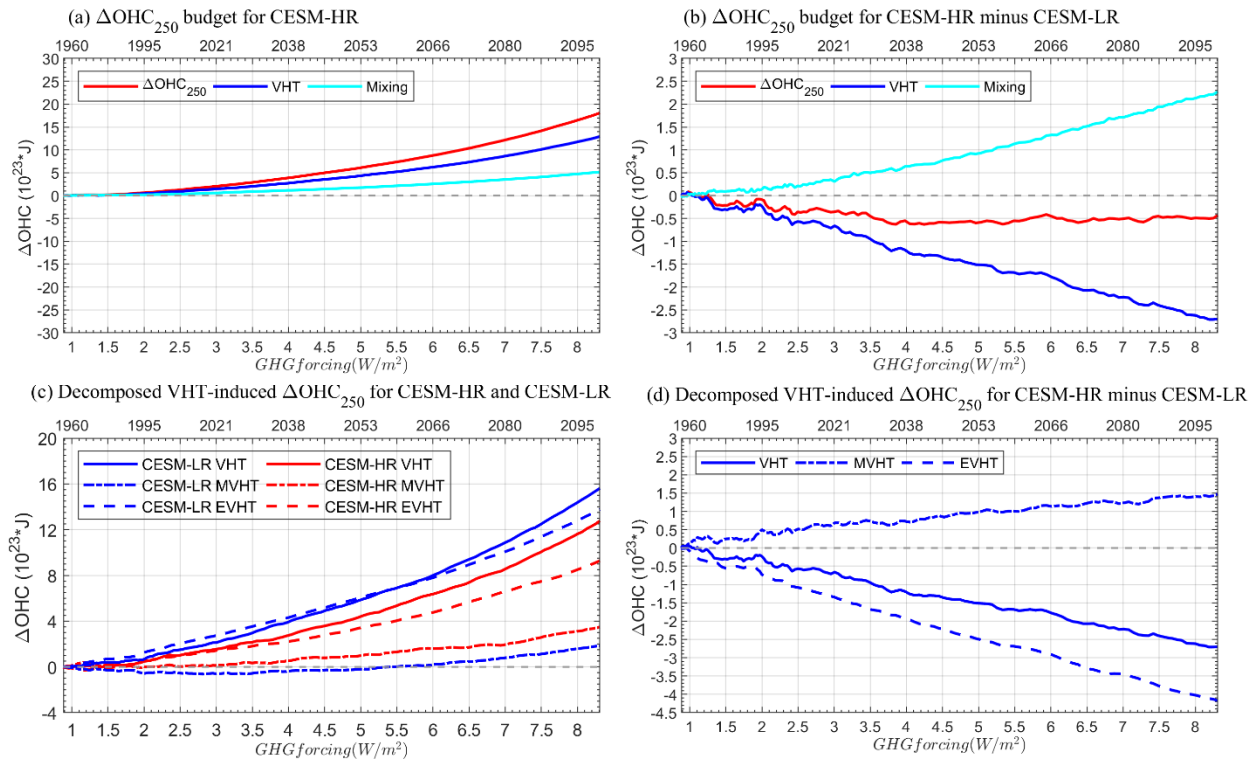
254 To further validate these CESM results, we analyze simulations from models participating in
255 CMIP5. Because the vertical heat redistribution can be influenced by both the atmospheric heat
256 input (i.e., the net surface heat flux) and vertical heat transport processes in the ocean, we here
257 show the temperature change (relative to the 1950-1960 mean) in the upper 250 m ($\Delta T_{250\text{m}}$) as a
258 function of total heat into the ocean, expressed as ocean temperature change, from 1950-2100
259 (Fig. 2e). Different models simulate different amounts of heat into the ocean at the end of year
260 2100 (end points of each line), ranging from 0.35°C to 0.78°C, which is primarily determined by
261 the respective models' climate sensitivity (Andrews et al., 2012; Zelinka et al., 2020). With the

262 same RCP8.5 forcing, ΔT_{250m} in CESM-HR lies outside of the spread of the CMIP5 ensemble,
 263 indicating that ΔT_{250m} projected by CESM-HR increases faster than not only CESM-LR but also
 264 all other non-eddy-resolving models.

265 **3.3 Role of resolved vs. parameterized eddy fluxes in vertical heat redistribution**

266 To further investigate why more heat is transported to the deep ocean in non-eddy-resolving
 267 simulations than in eddy-resolving simulations, we conduct a global-mean heat budget analysis
 268 below 250 m in CESM-HR and CESM-LR (Fig. 3), where the ocean temperature rises faster in
 269 CESM-LR than in CESM-HR without strong influences of internal variability at interannual-to-
 270 decadal timescales (Fig. 2c). A similar analysis can be applied to the upper 250 m except that the
 271 strong internal variability in the upper ocean makes the interpretation of the results more difficult.
 272 The integrated ΔOHC from 250 m to the bottom in CESM-HR, denoted as ΔOHC_{250} , shows a
 273 monotonic increase (red), primarily driven by the increase in VHT (blue) with a smaller
 274 contribution from the vertical turbulent mixing (cyan) (Fig. 3a). These two oceanic processes are
 275 responsible for transporting heat from the top 250 m into the deeper ocean. By the end of 2100,
 276 ΔOHC_{250} in CESM-HR is increased by 18×10^{23} J heat relative to 1950, roughly 72% of which is
 277 attributable to VHT.

278 Fig. 3b shows the difference in each term in the heat budget between CESM-HR and CESM-LR.
 279 ΔOHC_{250} is always smaller in CESM-HR than CESM-LR (red), indicating less warming below
 280 250 m in CESM-HR than in CESM-LR. This difference in ΔOHC_{250} between CESM-HR and
 281 CESM-LR is attributable to VHT, which transports less heat to the deep ocean in CESM-HR
 282 than CESM-LR. The vertical turbulent mixing induced ΔOHC_{250} difference between CESM-HR
 283 and CESM-LR significantly compensates the difference due to VHT.

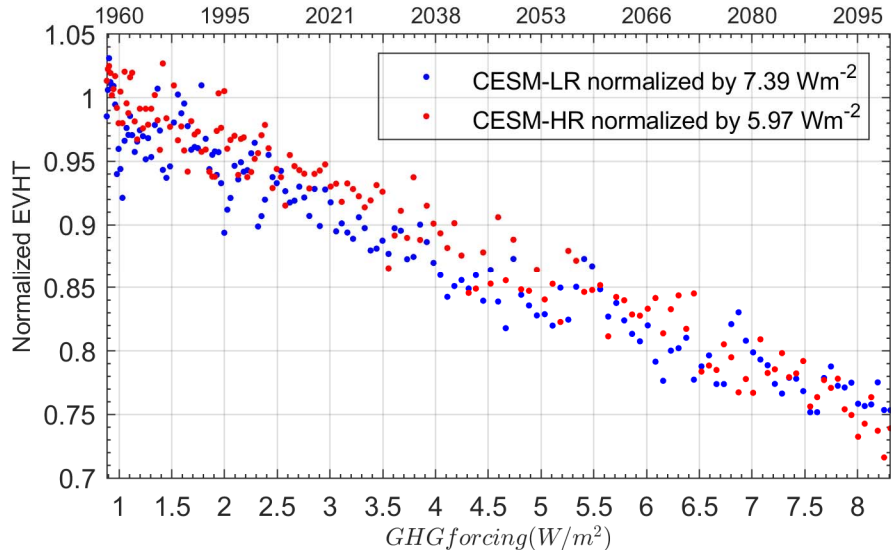


285 **Fig. 3. Globally averaged ΔOHC balance for the layer below 250 m.** Budget in (a) CESM-
 286 HR and (b) CESM-HR minus CESM-LR. In (a-b), red for ΔOHC_{250} , blue for VHT, and cyan for
 287 vertical mixing. (c) Decomposition of VHT-induced ΔOHC_{250} in CESM-HR (red) and CESM-
 288 LR (blue). (d) Differences in the decomposed VHT-induced ΔOHC_{250} between CESM-HR and
 289 CESM-LR. In (c-d), solid for total VHT, dot-dashed for MVHT, and dashed for EVHT.

290 Previous studies have shown that VHT results from the balance between upward EVHT and
 291 downward MVHT (Griffies et al., 2015; von Storch et al., 2016; Wolfe et al., 2008), which is
 292 also demonstrated in Fig. S4a. EVHT cools the layer below 250 m, while MVHT warms it. Fig.
 293 3c shows that as GHG emissions increase, the cooling effect of EVHT decreases, while the
 294 warming effect of MVHT increases. Both EVHT and MVHT lead to more heat being transported
 295 into the deep ocean by VHT (Fig. 3c). However, the difference in VHT change between CESM-
 296 HR and CESM-LR is mainly caused by the weaker reduction of EVHT in CESM-HR than in
 297 CESM-LR (Fig. 3d). At the same time, the downward MVHT increases faster in CESM-HR than
 298 in CESM-LR, which partially compensates for the CESM-HR and CESM-LR differences in
 299 EVHT changes by about 37% at the end of year 2100. Therefore, representations of EVHT in
 300 climate models are very important to accurately simulate future vertical heat distributions, as
 301 well as ocean stratification.

302 To understand the role of mesoscale eddy fluxes, it is important to note that they serve to stratify
 303 the ocean by slumping isopycnals, thereby reducing the available potential energy (Gent &
 304 McWilliams, 1990). In CESM-LR, the parameterized EVHT is represented by the Gent-
 305 McWilliams parameterization (GM) (Gent & McWilliams, 1990; Griffies, 1998), which depends
 306 on the thickness diffusivity controlled by ocean stratification, isopycnal slope, and horizontal
 307 temperature gradient. In PI-CNTL, CESM-LR simulations have weaker ocean stratification than
 308 CESM-HR simulations (Fig. S4b), which results in more available potential energy. Therefore,
 309 the global average of parameterized EVHT at 250 m in CESM-LR (7.39 Wm^{-2}) is larger than the
 310 resolved EVHT in CESM-HR (5.97 Wm^{-2}) when averaged over year 350-500 of PI-CNTL.

311 While the EVHT reduction in HF-TNST is weaker in CESM-HR than CESM-LR, this difference
 312 becomes much smaller after normalizing EVHT by their respective mean values in PI-CNTL
 313 (Fig. 4), indicating that GM represents similar percentage changes of mean EVHT in PI-CNTL
 314 in CESM-LR as in CESM-HR in response to GHG forcing. By the end of year 2100, both the
 315 parameterized (CESM-LR) and resolved (CESM-HR) EVHT are decreased by 25% relative to
 316 their respective mean values in PI-CNTL. This proportional relationship between future changes
 317 in EVHT and mean EVHT also holds at other depths where most mesoscale eddies are generated
 318 (Fig. S5). This result leads us to hypothesize that the different EVHT responses to GHG forcing
 319 between CESM-HR and CESM-LR, which have a significant impact on ocean stratification
 320 changes, may be directly related to the difference in the mean EVHT in PI-CNTL between
 321 CESM-HR and CESM-LR. The smaller mean EVHT in CESM-HR that corresponds to stronger
 322 ocean stratification and less available potential energy in PI-CTNL causes a proportionally
 323 weaker EVHT decrease in response to the future warming, resulting in more heat being trapped
 324 in the upper ocean, and thus stronger ocean stratification increase in CESM-HR compared to
 325 CESM-LR.



326

327 **Fig. 4. Globally averaged EVHT at 250 m in CESM-LR and CESM-HR.** EVHT at 250 m in
 328 CESM-LR (blue) and CESM-HR (red) are normalized by the respective mean in PI-CNTL.

329 4. Conclusions and Discussion

330 This study focuses on analyzing the vertical distribution of global mean ocean heat uptake
 331 specifically under the RCP8.5 high emission scenario. The analysis was conducted on an
 332 ensemble of CESM-HR simulations and compared to its CESM-LR counterpart. The results
 333 show that CESM-HR simulates stronger increase in upper-ocean stratification, even though the
 334 full-depth integrated ocean heat uptake is very similar between CESM-HR and CESM-LR. A
 335 comparison with other low-resolution climate model simulations participated in CMIP5 shows
 336 that this result holds for not only the CESM simulations, but also other models, suggesting that
 337 non-eddy-resolving climate models may underestimate the rate of future upper ocean
 338 stratification changes in response to GHG forcing. We would like to point out that with the same
 339 heat into the ocean, the upper ocean thermal stratification dT in CESM-HR increases faster than
 340 not only CESM-LR but also a vast majority of models participating in CMIP5 (Fig. S6).

341 A further comparative analysis of global-mean ocean heat budget reveals that the disparity in the
 342 upward EVHT serves as a major contributing factor to the divergence between CESM-HR and
 343 CESM-LR. The analysis demonstrates that CESM-LR exhibits a more rapid future decrease in
 344 EVHT, resulting in greater ocean heat uptake being transported into the deep ocean. We
 345 hypothesize that this discrepancy in EVHT response between CESM-HR and CESM-LR stems
 346 directly from the representation of mean EVHT in each model. In CESM-HR, the explicitly
 347 computed EVHT yields a smaller mean value compared to the parameterized EVHT in CESM-
 348 LR. This disparity corresponds to a stronger upper-ocean stratification and lower available
 349 potential energy in CESM-HR, potentially contributing to the comparatively weaker future
 350 decrease in EVHT when compared to CESM-LR. Further research is necessary to thoroughly
 351 examine and validate this hypothesis.

352 Acknowledgments

353 This research uses simulations performed by the International Laboratory for High-Resolution
354 Earth System Prediction (iHESP)—a collaboration among the Qingdao National Laboratory for
355 Marine Science and Technology (QNLN), Texas A&M University (TAMU), and the US
356 National Center for Atmospheric Research (NCAR). This research is partially supported by the
357 National Science Foundation (NSF) grant AGS-2231237 and the National Academies of Science
358 and Engineering (NASEM) Gulf Research Program grant 2000013283. NCAR is a major facility
359 sponsored by the US NSF under Cooperative Agreement 1852977. G. Xu and Q. Zhang
360 acknowledge the support from the China Scholarship Council. We thank TAMU
361 Supercomputing Facility and the Texas Advanced Computing Center (TACC) for providing the
362 computing resources for this research.

363

364 **Open Research**

365 Datasets from HF-TNST and PI-CNTL are available at
366 https://ihesp.github.io/archive/products/ihesp-products/data-release/DataRelease_Phase2.html.
367 CMIP5 data are available at <https://esgf-node.llnl.gov/search/cmip5/>. IAP ocean heat content is
368 available at
369 <http://www.ocean.iap.ac.cn/pages/dataService/dataService.html?navAnchor=dataService>. NOAA
370 ocean heat content is available at <https://www.ncei.noaa.gov/access/global-ocean-heat-content/>.
371 JMA ocean heat content is available at
372 https://www.data.jma.go.jp/gmd/kaiyou/english/ohc/ohc_global_en.html. Analyses were
373 conducted using Matlab.

374

375 **References:**

- 376 Andrews, T., Gregory, J. M., Webb, M. J., & Taylor, K. E. (2012). Forcing, feedbacks and
377 climate sensitivity in CMIP5 coupled atmosphere-ocean climate models. *Geophysical*
378 *Research Letters*, 39(9).
- 379 Bindoff, N. L., Cheung, W. W., Kairo, J. G., Arístegui, J., Guinder, V. A., Hallberg, R., et al.
380 (2019). Changing ocean, marine ecosystems, and dependent communities.
- 381 Bleuel, J., Pennino, M. G., & Longo, G. O. (2021). Coral distribution and bleaching vulnerability
382 areas in Southwestern Atlantic under ocean warming. *Scientific Reports*, 11(1), 1–12.
- 383 Bopp, L., Resplandy, L., Orr, J. C., Doney, S. C., Dunne, J. P., Gehlen, M., et al. (2013).
384 Multiple stressors of ocean ecosystems in the 21st century: projections with CMIP5
385 models. *Biogeosciences*, 10(10), 6225–6245.

- 386 Bourgeois, T., Goris, N., Schwinger, J., & Tjiputra, J. F. (2022). Stratification constrains future
387 heat and carbon uptake in the Southern Ocean between 30° S and 55° S. *Nature*
388 *Communications*, 13(1), 1–8.
- 389 Cantin, N. E., Cohen, A. L., Karnauskas, K. B., Tarrant, A. M., & McCorkle, D. C. (2010).
390 Ocean warming slows coral growth in the central Red Sea. *Science*, 329(5989), 322–325.
- 391 Capotondi, A., Alexander, M. A., Bond, N. A., Curchitser, E. N., & Scott, J. D. (2012).
392 Enhanced upper ocean stratification with climate change in the CMIP3 models. *Journal*
393 *of Geophysical Research: Oceans*, 117(C4).
- 394 Chang, P., Zhang, S., Danabasoglu, G., Yeager, S. G., Fu, H., Wang, H., et al. (2020). An
395 Unprecedented Set of High-Resolution Earth System Simulations for Understanding
396 Multiscale Interactions in Climate Variability and Change. *Journal of Advances in*
397 *Modeling Earth Systems*, 12(12), e2020MS002298.
398 <https://doi.org/10.1029/2020MS002298>
- 399 Chang, P., Xu, G., Kurian, J., Small, R. J., Danabasoglu, G., Yeager, S., et al. (2023). Uncertain
400 future of sustainable fisheries environment in eastern boundary upwelling zones under
401 climate change. *Communications Earth & Environment*, 4(1), 19.
- 402 Chen, X., & Tung, K.-K. (2014). Varying planetary heat sink led to global-warming slowdown
403 and acceleration. *Science*, 345(6199), 897–903.
- 404 Cheng, L., Trenberth, K. E., Fasullo, J., Boyer, T., Abraham, J., & Zhu, J. (2017). Improved
405 estimates of ocean heat content from 1960 to 2015. *Science Advances*, 3(3), e1601545.
- 406 Cheng, L., Abraham, J., Hausfather, Z., & Trenberth, K. E. (2019). How fast are the oceans
407 warming? *Science*, 363(6423), 128–129.

- 408 Church, J. A., White, N. J., Konikow, L. F., Domingues, C. M., Cogley, J. G., Rignot, E., et al.
409 (2011). Revisiting the Earth's sea-level and energy budgets from 1961 to 2008.
410 *Geophysical Research Letters*, 38(18).
- 411 Domingues, C. M., Church, J. A., White, N. J., Gleckler, P. J., Wijffels, S. E., Barker, P. M., &
412 Dunn, J. R. (2008). Improved estimates of upper-ocean warming and multi-decadal sea-
413 level rise. *Nature*, 453(7198), 1090–1093.
- 414 Flato, G., Marotzke, J., Abiodun, B., Braconnot, P., Chou, S. C., Collins, W., et al. (2013).
415 Evaluation of climate models. In *Climate change 2013: the physical science basis. Contribution of Working Group I to the Fifth Assessment Report of the Intergovernmental*
416 *Panel on Climate Change* (pp. 741–866). Cambridge, United Kingdom and New York,
417 NY, USA: Cambridge University Press.
- 419 Fox-Kemper, B., Ferrari, R., & Hallberg, R. (2008). Parameterization of mixed layer eddies. Part
420 I: Theory and diagnosis. *Journal of Physical Oceanography*, 38(6), 1145–1165.
- 421 Frieler, K., Meinshausen, M., Golly, A., Mengel, M., Lebek, K., Donner, S., & Hoegh-Guldberg,
422 O. (2013). Limiting global warming to 2 C is unlikely to save most coral reefs. *Nature*
423 *Climate Change*, 3(2), 165–170.
- 424 Fu, W., Randerson, J. T., & Moore, J. K. (2016). Climate change impacts on net primary
425 production (NPP) and export production (EP) regulated by increasing stratification and
426 phytoplankton community structure in the CMIP5 models. *Biogeosciences*, 13(18), 5151–
427 5170.
- 428 Gattuso, J.-P., Magnan, A., Billé, R., Cheung, W. W., Howes, E. L., Joos, F., et al. (2015).
429 Contrasting futures for ocean and society from different anthropogenic CO₂ emissions
430 scenarios. *Science*, 349(6243), aac4722.

- 431 Gent, P. R., & McWilliams, J. C. (1990). Isopycnal mixing in ocean circulation models. *Journal*
432 *of Physical Oceanography*, 20(1), 150–155.
- 433 Griffies, S. M. (1998). The gent–mcwilliams skew flux. *Journal of Physical Oceanography*,
434 28(5), 831–841.
- 435 Griffies, S. M., Winton, M., Anderson, W. G., Benson, R., Delworth, T. L., Dufour, C. O., et al.
436 (2015). Impacts on ocean heat from transient mesoscale eddies in a hierarchy of climate
437 models. *Journal of Climate*, 28(3), 952–977.
- 438 Helm, K. P., Bindoff, N. L., & Church, J. A. (2011). Observed decreases in oxygen content of
439 the global ocean. *Geophysical Research Letters*, 38(23).
- 440 Ishii, M., Fukuda, Y., Hirahara, S., Yasui, S., Suzuki, T., & Sato, K. (2017). Accuracy of global
441 upper ocean heat content estimation expected from present observational data sets. *Sola*,
442 13, 163–167.
- 443 Keeling, R. F., Körtzinger, A., & Gruber, N. (2010). Ocean deoxygenation in a warming world.
444 *Annu. Rev. Mar. Sci*, 2(1), 199–229.
- 445 Kuhlbrodt, T., & Gregory, J. (2012). Ocean heat uptake and its consequences for the magnitude
446 of sea level rise and climate change. *Geophysical Research Letters*, 39(18).
- 447 Levitus, S., Antonov, J. I., Boyer, T. P., Baranova, O. K., Garcia, H. E., Locarnini, R. A., et al.
448 (2012). World ocean heat content and thermosteric sea level change (0–2000 m), 1955–
449 2010. *Geophysical Research Letters*, 39(10).
- 450 Li, G., Cheng, L., Zhu, J., Trenberth, K. E., Mann, M. E., & Abraham, J. P. (2020). Increasing
451 ocean stratification over the past half-century. *Nature Climate Change*, 10(12), 1116–
452 1123.

- 453 Meehl, G. A., Yang, D., Arblaster, J. M., Bates, S. C., Rosenbloom, N., Neale, R., et al. (2019).
454 Effects of model resolution, physics, and coupling on Southern Hemisphere storm tracks
455 in CESM1. 3. *Geophysical Research Letters*, *46*(21), 12408–12416.
- 456 Moore, J. K., Fu, W., Primeau, F., Britten, G. L., Lindsay, K., Long, M., et al. (2018). Sustained
457 climate warming drives declining marine biological productivity. *Science*, *359*(6380),
458 1139–1143.
- 459 Perry, A. L., Low, P. J., Ellis, J. R., & Reynolds, J. D. (2005). Climate change and distribution
460 shifts in marine fishes. *Science*, *308*(5730), 1912–1915.
- 461 Pinsky, M. L., Worm, B., Fogarty, M. J., Sarmiento, J. L., & Levin, S. A. (2013). Marine taxa
462 track local climate velocities. *Science*, *341*(6151), 1239–1242.
- 463 Rhein, M., Rintoul, S., Aoki, S., Campos, E., Chambers, D., Feely, R., et al. (2013).
464 Observations: Ocean. In *Climate change 2013: the physical science basis. Contribution*
465 *of Working Group I to the Fifth Assessment Report of the Intergovernmental Panel on*
466 *Climate Change* (Vol. 1). Cambridge, United Kingdom and New York, NY, USA:
467 Cambridge University Press.
- 468 Roberts, M. J., Baker, A., Blockley, E. W., Calvert, D., Coward, A., Hewitt, H. T., et al. (2019).
469 Description of the resolution hierarchy of the global coupled HadGEM3-GC3. 1 model as
470 used in CMIP6 HighResMIP experiments. *Geoscientific Model Development*, *12*(12),
471 4999–5028.
- 472 Schmidtko, S., Stramma, L., & Visbeck, M. (2017). Decline in global oceanic oxygen content
473 during the past five decades. *Nature*, *542*(7641), 335–339.

- 474 Small, R. J., Bacmeister, J., Bailey, D., Baker, A., Bishop, S., Bryan, F., et al. (2014). A new
475 synoptic scale resolving global climate simulation using the Community Earth System
476 Model. *Journal of Advances in Modeling Earth Systems*, 6(4), 1065–1094.
- 477 von Storch, J.-S., Haak, H., Hertwig, E., & Fast, I. (2016). Vertical heat and salt fluxes due to
478 resolved and parameterized meso-scale eddies. *Ocean Modelling*, 108, 1–19.
- 479 Trenberth, K. E., Fasullo, J. T., & Balmaseda, M. A. (2014). Earth’s energy imbalance. *Journal*
480 *of Climate*, 27(9), 3129–3144.
- 481 Wills, R. C., Battisti, D. S., Armour, K. C., Schneider, T., & Deser, C. (2020). Pattern
482 recognition methods to separate forced responses from internal variability in climate
483 model ensembles and observations. *Journal of Climate*, 33(20), 8693–8719.
- 484 Wolfe, C. L., Cessi, P., McClean, J. L., & Maltrud, M. E. (2008). Vertical heat transport in
485 eddying ocean models. *Geophysical Research Letters*, 35(23).
- 486 Yamaguchi, R., & Suga, T. (2019). Trend and variability in global upper-ocean stratification
487 since the 1960s. *Journal of Geophysical Research: Oceans*, 124(12), 8933–8948.
- 488 Zelinka, M. D., Myers, T. A., McCoy, D. T., Po-Chedley, S., Caldwell, P. M., Ceppi, P., et al.
489 (2020). Causes of higher climate sensitivity in CMIP6 models. *Geophysical Research*
490 *Letters*, 47(1), e2019GL085782.

491



Geophysical Research Letters

Supporting Information for

Enhanced upper ocean warming projected by the eddy-resolving Community Earth System Model

Gaopeng Xu¹, Ping Chang^{1,2}, Justin Small³, Gokhan Danabasoglu³, Stephen Yeager³, Sanjiv Ramachandran¹, and Qiuying Zhang¹

¹Department of Oceanography, Texas A&M University, College Station, Texas, USA

²Department of Atmospheric Sciences, Texas A&M University, College Station, Texas, USA

³National Center for Atmospheric Research, Boulder, Colorado, USA.

Contents of this file

Figures S1 to S6

Tables S1

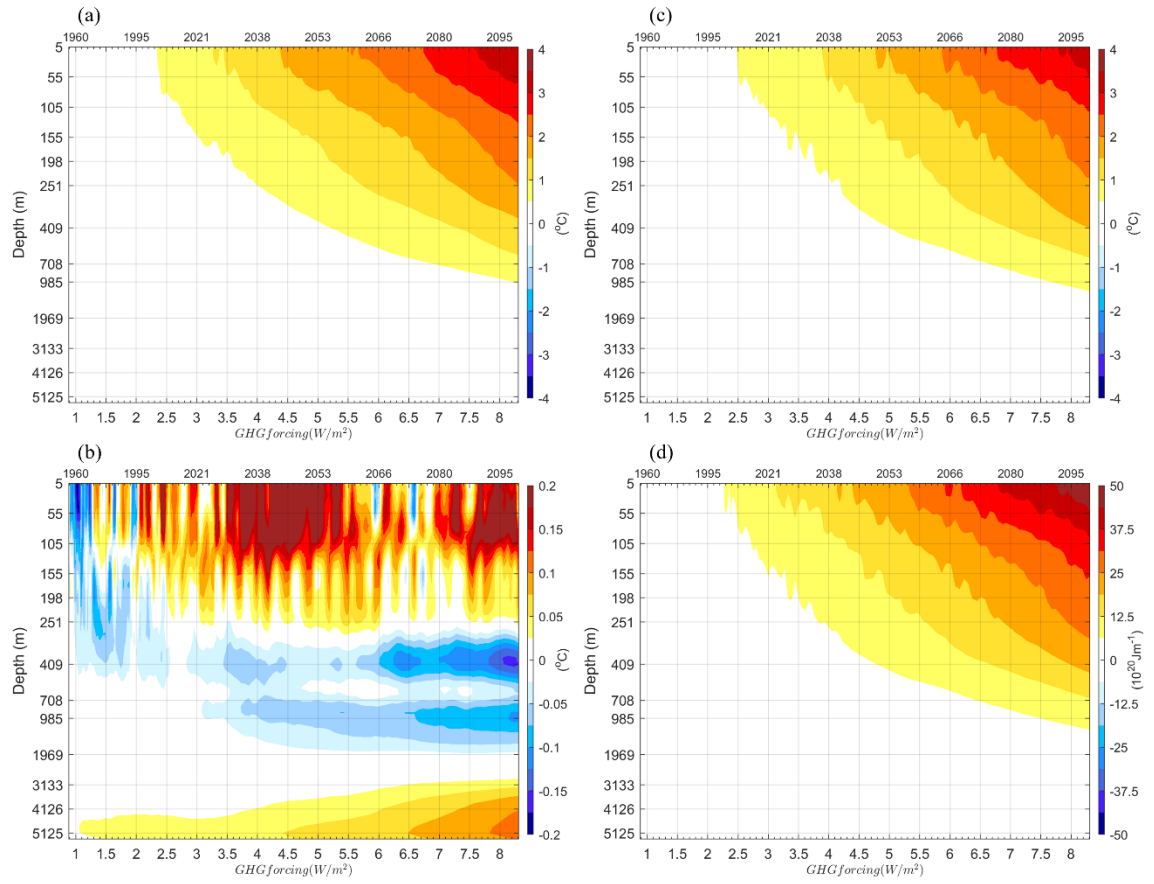


Fig. S1. (a-b) same results as those in Fig.2b-c, respectively, but not scaled with horizontal ocean area, c_p and ρ_0 . (c-d) Temperature changes in CESM-LR with the unit of $^{\circ}C$ and $10^{20} Jm^{-1}$, respectively.

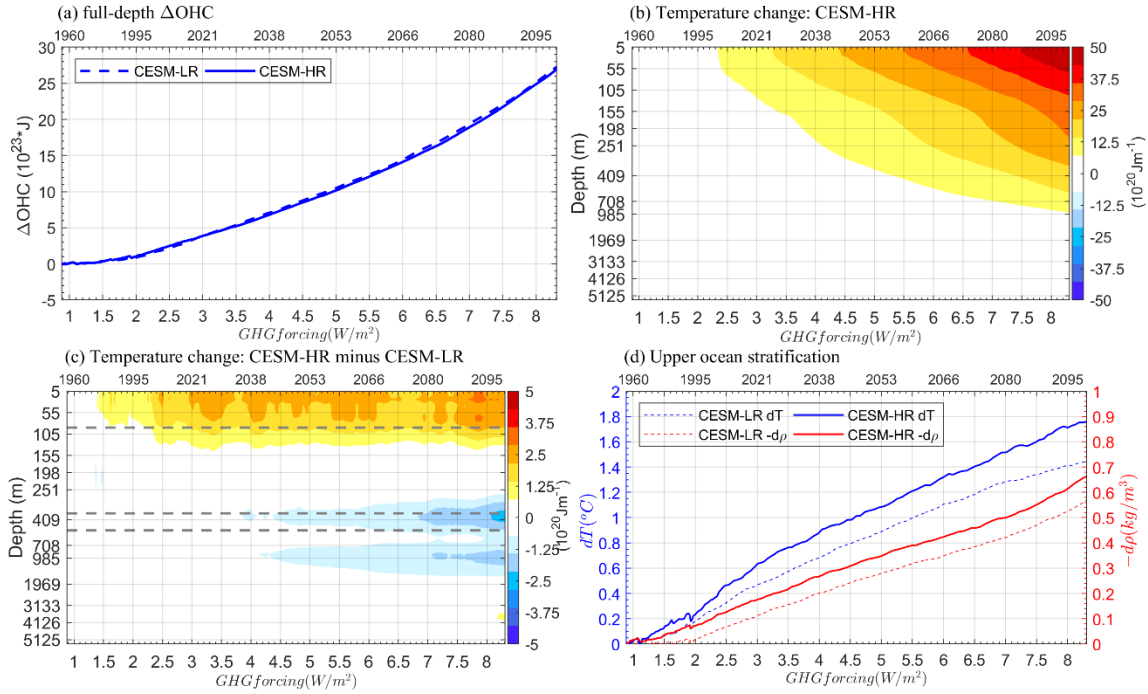


Fig. S2. Similar to Fig. 2a-d, but signal-to-noise maximizing EOF is applied to global-mean temperature and density as a function of depth and time. The forced patterns are chosen with more than 70% explained total variance.

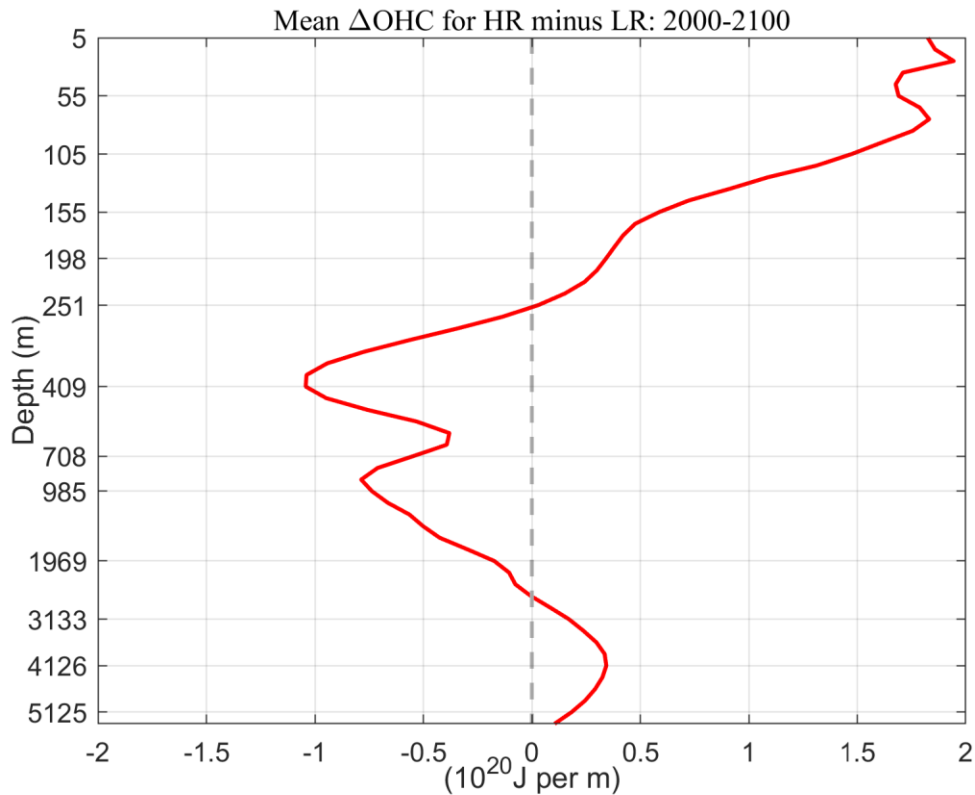


Fig. S3. Mean CESM-HR and -LR difference in ΔOHC over 2000-2100.

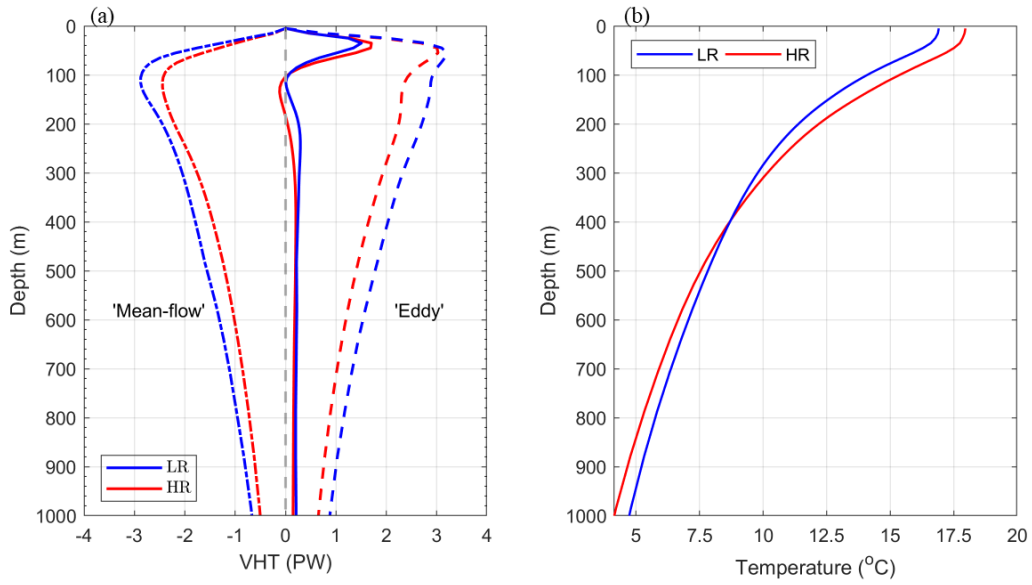


Fig. S4. Vertical profiles of globally-averaged vertical heat transport fluxes (a) and temperature (b) in CESM-LR (blue) and CESM-HR (red) PI-CNTL averaged over year 350-500. In (a), solid for total VHT, dot-dashed for MVHT, and dashed for EVHT.

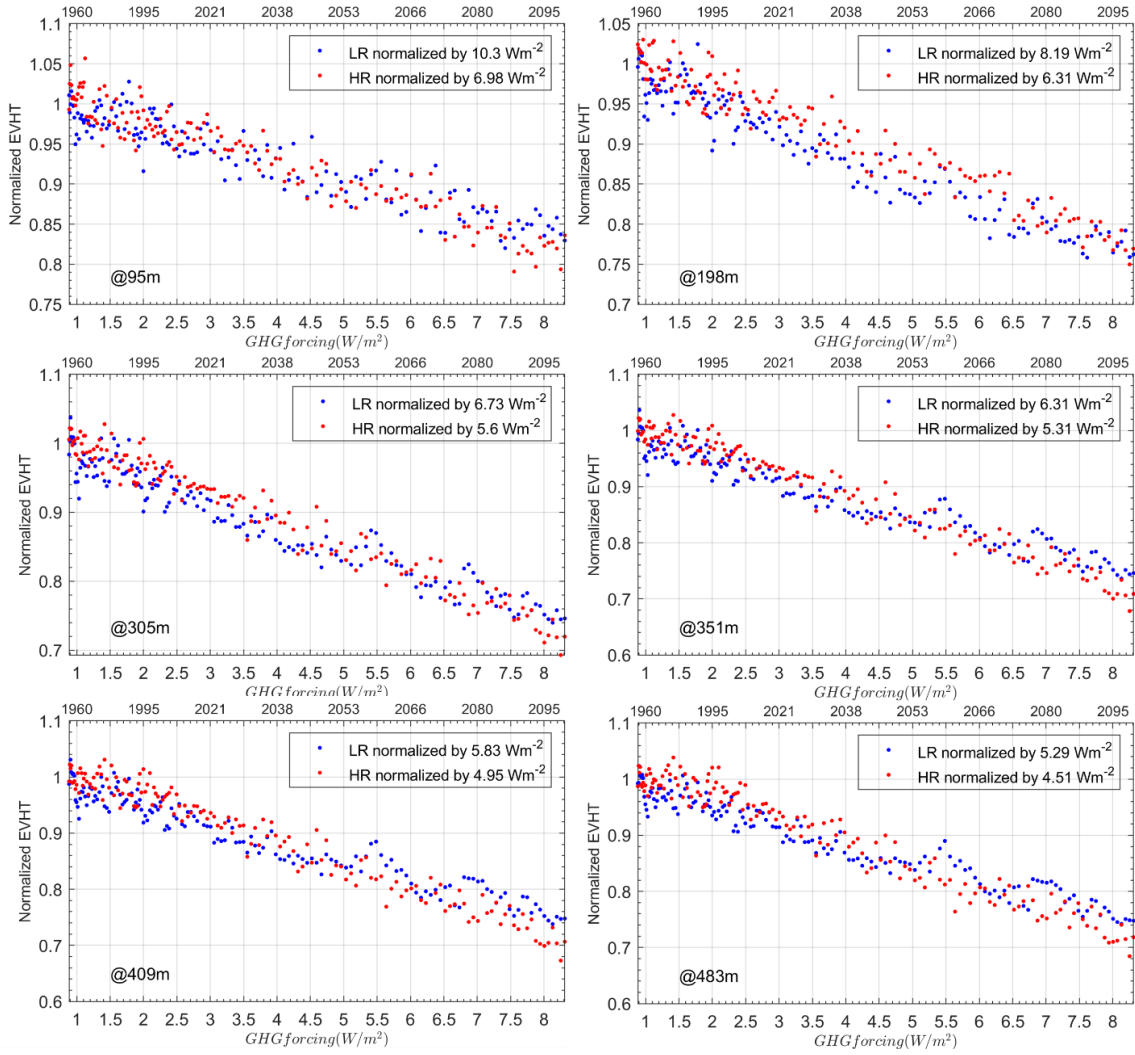


Fig. S5. Similar to Fig. 4, but at different depths.

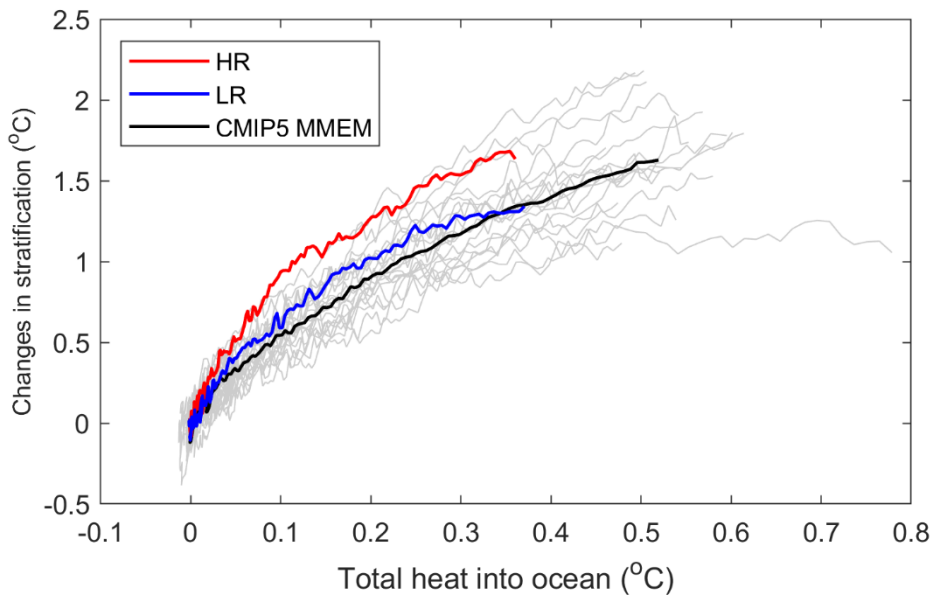


Fig. S6. Changes in dT in CMIP5.

Table S1. Model information of 20 models included in CMIP5 simulations.

Model name	Nation	Atmospheric model Atmosphere resolution	Ocean model Ocean resolution
ACCESS1-0	Australia	HadGEM2 r1.1 N96 ($\sim 1.875^\circ \times 1.25^\circ$); 38 levels	MOM4p1 Nominal $1^\circ \times 1^\circ$; 50 levels
ACCESS1-3	Australia	Global Atmosphere 1.0 N96 ($\sim 1.875^\circ \times 1.25^\circ$); 38 levels	MOM4p1 Nominal $1^\circ \times 1^\circ$; 50 levels
BCC-CSM1-1	China	BCC-AGCM2.1 T42 ($2.8125^\circ \times 2.8125^\circ$); 26 levels	MOM4-L40v1 Nominal $1^\circ \times 1^\circ$; 40 levels
CanESM2	Canada	CanAM4 $\sim 2.8^\circ \times 2.8^\circ$; 35 levels	CanOM4 256 x 192 longitude/latitude; 40 levels
CESM1-CAM5	USA	CAM5 $\sim 1.25^\circ \times 0.9^\circ$; 30 levels	POP2 320 x 384 longitude/latitude; 60 levels
CMCC-CESM	Italy	ECHAM5 T159 ($0.75^\circ \times 0.75^\circ$); 31 levels	OPA8.2 2° average, 0.5° at the equator; 31 levels
CMCC-CM	Italy	ECHAM5 T159 ($0.75^\circ \times 0.75^\circ$); 31 levels	OPA8.2 2° average, 0.5° at the equator; 31 levels
CMCC-CMS	Italy	ECHAM5 T65 ($0.75^\circ \times 0.75^\circ$); 95 levels	OPA8.2 2° average, 0.5° at the equator; 31 levels
CNRM-CM5	France	ARPEGE-Climat V5.2.1 T127 ($\sim 1.4^\circ \times 1.4^\circ$); 31 levels	NEMO 3.2 $\sim 1^\circ \times 1^\circ$; 42 levels
CSIRO-Mk3-6-0	Australia	AGCM v7.3.4 T63 ($\sim 1.875^\circ \times 1.875^\circ$); 18 levels	MOM2.2 $\sim 1.875^\circ \times 0.9375^\circ$; 31 levels
FGOALS-s2	China	SAMIL2 R42 ($\sim 1.66^\circ \times 2.81^\circ$); 26 levels	LICOM2 $\sim 1^\circ \times 1^\circ$; 42 levels, 31 levels

Model name	Nation	Atmospheric model Atmosphere resolution	Ocean model Ocean resolution
GFDL-CM3	USA	AM3 2.5° x 2°; 48 levels	MOM4p1 Tripolar 360 x 200; 50 levels
HadGEM2-ES	UK	HadGAM2 N96 (1.875°x1.25°); 38 levels	HadGOM2 1° longitude x 0.3° to 1° latitude; 40 levels
IPSL-CM5A-LR	France	LMDZ5 95 x 96 equivalent to 3.75°x1.9°; 39 levels	NEMO 3.2 2° longitude x 0.5° to 2° latitude; 31 levels
IPSL-CM5A-MR	France	LMDZ5 143 x 144 equivalent to 1.25°x2.5°; 39 levels	NEMO 3.2 2° longitude x 0.5° to 2° latitude; 31 levels
IPSL-CM5B-LR	France	LMDZ5 95 x 96 equivalent to 3.75°x1.9°; 39 levels	NEMO 3.2 2° longitude x 0.5° to 2° latitude; 31 levels
MIROC-ESM-CHEM	Japan	MIROC-AGCM6 T85 (1.40625°x1.40625°); 40 levels	COCO4.5 1.4° longitude x 0.5°-1.4° latitude; 50 levels
MIROC-ESM	Japan	MIROC-AGCM T42 (2.8125°x2.8125°); 80 levels	COCO3.4 1.4° longitude x 0.5°-1.4° latitude; 44 levels
MPI-ESM-LR	Germany	ECHAM6 T63 (~1.8°x1.8°); 47 levels	MPIOM Average 1.5°; 40 levels
MPI-ESM-MR	Germany	ECHAM6 T63 (~1.8°x1.8°); 95 levels	MPIOM ~0.4°x 0.4°; 40 levels